Published in final edited form as:

J Biomed Mater Res B Appl Biomater. 2022 February ; 110(2): 422–430. doi:10.1002/jbm.b.34918.

Tranexamic acid-loaded hemostatic nanoclay microsphere frameworks

Isabelle Denry[1,2,3], **Jean-Marie Nédélec**[3], **Julie A. Holloway**[2]

[1]Iowa Institute for Oral Health Research, University of Iowa College of Dentistry, Iowa City, Iowa, USA

[2]Department of Prosthodontics, University of Iowa College of Dentistry, Iowa City, Iowa, USA

[3]Université Clermont Auvergne, Clermont Auvergne INP, CNRS, ICCF, Clermont-Ferrand, France

Abstract

Fast acting topical hemostatic agents play a key role in hemorrhage control. Retarding fibrinolysis is also critical in improving coagulation, thereby expanding chances of survival. The purpose of the present work was to investigate the physical properties, loading capacity and hemostatic efficacy of newly developed nanoclay microsphere frameworks (NMFs) loaded with tranexamic acid (TA), as antifibrinolytic agent. Nanoclay compositions were prepared with increasing levels of TA. Results showed that TA was successfully incorporated into the nanoclay structure and released when solvated with ethanol. Both doped and undoped NMFs significantly decreased activated partial thromboplastin time and increased clot stiffness, which was attributed to significantly thinner fibrin fibers and a denser clot structure.

Keywords

clotting time; hemostasis; nanoclay; topical hemostatic agent; tranexamic acid

1 | INTRODUCTION

Topical hemostatic agents (THAs) are commonly used to control severe bleeding in both military and civilian prehospital care.[1,2] Over the past decades, their use has increased significantly in patients undergoing major surgical procedures, such as cardiothoracic or orthopedic surgery.[3] In oral and maxillofacial surgery, the presence of a robust vascular supply and the fact that wounds are not amenable to control by tourniquet placement, further warrant the use of THAs.[4] To this effect, a large variety of hemostatic products is currently proposed, from scaffold or matrix agents to biological hemostats, stryptics, tissue sealants, tissue adhesives, and occlusive agents. However, scaffold agents present several drawbacks, such as cost (microfibrillar collagen, microporous mucopolysaccharide microspheres), delayed action (gelatin foam), lack of biodegradability (oxidized and regenerated cellulose),

Correspondence: Isabelle Denry, Université Clermont-Auvergne, Clermont Auvergne INP, Clermont-Ferrand, France. isabelle-denry@uiowa.edu.

CONFLICT OF INTEREST

The authors declare no conflict of interest.

while biological hemostats such as fibrin and thrombin do not rule out the potential for viral transmission.

Inorganic THAs, such as zeolites and clays have long drawn interest, as they are easily prepared and free of animal or human-derived proteins. Specifically, nanoclay minerals stand out as candidates of choice for the control of hemostasis due to their unique crystallographic configuration.[5] Clays are hydrated silicates with a layered structure leading to a higher specific surface area (SSA) than that of chain silicates, and a net surface charge that can be positive or negative, depending on chemistry. For example, kaolin layers consist of a sheet of silicon tetrahedrally coordinated to oxygen atoms and a sheet of aluminum octahedrally coordinated to both oxygen and hydroxyl groups, which gives kaolin a net negative surface charge at the pH of blood. This leads to the autocatalytic activation of coagulation factors XII and XI, and subsequently, the initiation of the intrinsic pathway of coagulation.[6] As a result, kaolin is routinely used as a clotting initiator in clinical assays. Kaolin-impregnated gauze is used as THA and was FDA-approved in 2013 for external application.[7,8] Meanwhile, synthetic smectite nanoclays (Laponite RD) have recently attracted interest due to their potential as drug delivery systems.[9] These clay particles are nanosized discs (25 nm diameter; 1–2 nm thick) negatively charged on their faces, with positively charged rims. They undergo complete dissociation by osmotic swelling when mixed with water. Due to their anisotropic charge, they form self-assembled structures that lead to a shear-thinning gel as they form and break. The cationic interlayer in the synthetic laponite (LAP) lamellar structure, can be intercalated with therapeutic agents or amino acids, making it an ideal carrier to promote wound healing.[10] Moreover, LAP platelets have been tested in an array of potential applications such as osteogenic agents,[11] drug delivery agents,[12,13] or injectable hemostatic hydrogels.[14] LAP nanodiscs ($Na_{0.7}Mg_{5.5}Li_{0.3}Si_8O_{20}(OH)_4$) have been shown to degrade into nontoxic by-products in physiological conditions[15] and exhibit excellent biocompatibility with both human and animal cells.[11,16]

As mentioned earlier, LAP nanodiscs can self-assemble into inter-locked plate-like microstructures when dispersed in water due to their anisotropic charge.[15,17] We have recently discovered that by spraying LAP dispersions, we were able to produce self-assembled silicate nanoclay microsphere frameworks (NMFs) with honeycomb-like pores in the 3–6 μm range, well-suited to promote physical blood cell concentration, in addition to triggering the intrinsic pathway of coagulation, similarly to kaolin. Meanwhile, antifibrinolytics such as tranexamic acid (TA) are widely used to treat hemophilia and other coagulopathies.[18] These drugs are able to prevent the breakdown of the clot. TA works by binding to plasminogen and prevents it from reacting with fibrin, thereby avoiding fibrinolysis.[19] It has been FDA-approved as an antifibrinolytic agent since 1986 and is readily available.[18] However, THAs with antifibrinolytic properties have been seldom reported, while the combination of hemostatic and antifibrinolytic properties is highly desirable to efficiently stop hemorrhages. For clinical use as THAs, these loaded NMFs could easily be incorporated into a gauze as are zeolite components in materials such as Quikclot Combat Gauze. They could also be applied topically as a powder similarly to polysaccharide-based microspheres such as Arista (C. R. Bard) since, as mentioned earlier, LAP nanoclay compounds are both resorbable and biocompatible.

The purpose of the present work was to explore the drug loading capacity of LAP nanoclay microspheres with TA and to investigate the effect of TA loading on their physical properties and hemostatic efficacy.

2 | MATERIALS AND METHODS

2.1 | NMFs preparation

Four compositions with increasing amounts of TA were prepared by first dispersing 2 wt% Laponite RD powder (Rockwood Additives, Ltd.) in ultrapure water under stirring for 2 hr. Reagent grade TA (Sigma-Aldrich) was then added in concentrations of 2.5, 4, and 5 mg ml^{-1}, ($LTA_{2.5}$, LTA_4, LTA_5) and mixed for 48 hr at room temperature. A dispersion without TA addition (L_0) served as control. Dispersions were then freeze-sprayed and immediately freeze-dried for 48 hr.

2.2 | Powder characterization

Powder particles were examined by both optical microscopy and scanning electron microscopy (SEM). A series of micrographs was collected for each composition. Particle diameters ($n = 400$) were measured on digital micrographs ($n = 4$ per group) using NIH ImageJ software (version 1.8.0; public domain).[20] Particle distribution frequencies were fitted assuming a log normal distribution. A microporous starch-based commercially available THA, also presenting under the form of microspheres (Arista, C. R. Bard), was used as control material.

Differential thermal analyses (DTAs) were performed under nitrogen gas flow on the various powders recovered from freeze-drying, to investigate the thermal behavior (Model: Q600 DTA/TGA, TA Instruments). Analyses were performed at a heating rate of 40°C/min up to 1,300°C. Aluminum oxide (99.99%) powder served as reference standard. Crystal-line phases were characterized by X-ray diffraction (XRD). Scans were performed in the two-theta range 2–65°, at 40 kV and 44 mA in Bragg–Brentano configuration (SmartLab, Rigaku Americas). Peak positions were determined using PDXL-2 analysis software (PDXL-2, Rigaku Americas) after calibration using an internal silicon powder standard (NIST, SRM 640d). Both dry and ethanol-solvated specimens were analyzed in order to assess the eventual release of TA. The SSA was determined according to the Brunauer–Emmett–Teller (BET) approach using a Micro-meritics Tristar apparatus under liquid nitrogen at 77 K after degassing at 120°C under vacuum for 18 hr. The SSA was calculated from the N_2 adsorption isotherm using the BET equation.

2.3 | Quantification of TA release by ultraviolet–visible spectrometry

The amount of TA released from the powders was measured by ultraviolet–visible (UV–vis) spectrometry using ninhydrin as a reagent. The technique relies on the fact that TA contains a primary aliphatic amino group that reacts with ninhydrin via oxidation deamination of this group in phosphate buffer at pH 8. This reaction is accompanied with the development of a deep purple color also known as Ruhemann's purple. First, a calibration curve was established according to the technique proposed by Ansari et al.[21] Next 10 mg of powder for each composition were dissolved in 1 ml of ultrapure water, vortexed for 30 s and

centrifuged at 15,000 rpm for 10 min. After incubation with phosphate buffer and ninhydrin at 90°C for 20 min,[21] absorption spectra of the supernatant were recorded with 10 mm optical path length quartz cuvettes using an UV–vis spectrometer (Cary 50, Varian). TA concentrations for each composition were calculated with the linear regression equation obtained from the calibration curve.

2.4 | Activated partial thromboplastin time

The activated partial thromboplastin time (aPTT) was determined using a semiautomatic coagulation analyzer (BFT II, Siemens) and recommended reagents, including platelet poor plasma (PPP; Control Plasma P, Siemens), aPTT reagent (Actin FSL, Siemens) and 0.2 M calcium chloride ($CaCl_2$ solution, Siemens). Solutions of NMFs at concentrations of 25 mg ml^{-1} were prepared and vortexed for 30 s. All test samples ($n = 5$ per composition), cuvettes and test reagents were incubated at 37°C. Next, 50 μl of PPP and 50 μl of NMF solution were added to the cuvette and incubated at 37°C for 3 min. Finally, 50 μl of $CaCl_2$ were added after incubation. As soon as clotting was detected, the clotting time was displayed and recorded. PPP and aPTT reagent were used as negative control. Arista hemostatic agent was used as positive control. Standard reagents and control plasma were used to establish control aPTT.

2.5 | Coagulation profile by thromboelastography

Coagulation profiles were collected using a thromboelastograph (TEG 5000, Haemonetics). The instrument was calibrated with citrated platelet rich bovine plasma containing tissue factor (Factor III) with two levels of clot strength (Level I and II Control Plasma, Haemonetics). Test samples ($n = 3$) were prepared by mixing 4 mg of NMF with 340 ml of Level I control plasma. Coagulation profiles were recorded after adding 20 ml of 0.2 M $CaCl_2$. Specific parameters representing the three phases of the cell-based model of hemostasis (*R*, *k*, *a* angle, *MA*, *G*, and coagulation index [CI]) were collected. *R* is the reaction time for formation of the first levels of detectable clot formation and represents the enzymatic portion of coagulation. *K* is the time to reach a fixed level of clot strength (amplitude of 22 mm) and represents initial clot kinetics. The angle *a* measures the rapidity of fibrin buildup and cross linking as the clot strengthens and represents fibrinogen level. Maximum amplitude (MA) is a direct function of clot strength and is reflective of platelet function. *G* is the shear elastic modulus strength and expresses clot firmness while the CI is an overall assessment of coagulability.[22] Arista was used as positive control, Level I plasma after addition of calcium chloride was used as a standard.

2.6 | SEM of fibrin network

Fibrin formation within PPP mixed with NMFs was observed by SEM. Level I PPP (340 μl) was mixed with 4 mg of NMFs in an Eppendorf test tube, and 20 μl of $CaCl_2$ (0.2 M) were added. Samples were dip rinsed twice in phosphate buffered solution (PBS) to remove uncoagulated plasma and fixed with 2.5% glutaraldehyde solution (1 ml) for 15 min, followed by classical dehydration using graded series of ethanol solutions. After drying for 12 hr at 37°C and sputter-coating with gold, samples were observed by SEM (Hitachi-4800, Hitachi, Japan). Four images at 10,000× were selected per each experimental group and

the diameter of 150 randomly selected fibrin fibers were measured using NIH ImageJ software.[20]

2.7 | Statistical analyses

Means for particle size and fibrin fiber diameter were compared using Kruskal–Wallis test combined with the modification of Tukey's adjustment for multiple pairwise comparisons as explained by Conover,[23] in conjunction with an overall 0.05 level of Type I error. Means for other variables were tested by analysis of variance with Tukey's adjustment for multiple pairwise comparisons. A p-value of less than .05 was considered statistically significant.

3 | RESULTS

Representative SEMs of NMF particles and particle frequency distributions are shown in Figure 1. All nanoclay microspheres exhibited a fine honeycomb microarchitecture with a pore size in the range 3–6 μm. The pore structure is particularly well defined on microspheres that have been partially compressed to expose the inner core. Higher magnifications micrographs of a compressed microsphere revealing the fine honeycomb microstructure are shown in Figure 2. The mean particle size for composition $LTA_{2.5}$ (89.5 ± 27.7 μm) was significantly higher than that of all other groups ($p < .0001$). Meanwhile, the mean particle size for Arista (control THA) was significantly smaller (54.4 ± 18.5 μm) compared to all other groups. In addition, Arista particles did not exhibit open porosity. Particle frequencies followed a log normal distribution for all groups.

DTAs are shown in Figure 3. All nanoclay compositions thermo-grams exhibited an exotherm in the 780–784°C range. An endotherm was also present in the 449–461°C range for TA-containing nanoclay compositions. Arista control only showed an endotherm at 300°C.

XRD patterns are displayed in Figure 4a,b. Patterns in Figure 4a correspond to raw dry powders, patterns in Figure 4b correspond to powders solvated with ethanol and dried at room temperature for 30 min. Measured basal interlayer d_{001} spacings are listed in Table 1. There was an increase in d_{001} interlayer spacing with increasing TA loading in nanoclay compositions. Mixing the powder with ethanol did not significantly affect the d_{001} interlayer spacing for TA-free composition L_0. However, d_{001} decreased for all TA-loaded compositions, together with the appearance of reflections corresponding to TA, the intensity of which increased with TA loading. SSA measurements from BET adsorption profiles are summarized in Table 1. The SSA was between six and eight times lower for TA-loaded compositions, compared to the TA-free composition (L_0).

The UV–vis calibration curve for TA is shown in Figure 5a. Although a second absorption peak was observed at 400 nm, absorbance measurements were made at 565 nm, as recommended in the spectrophotometric protocol described by Ansari et al.[21] The corresponding linear regression is shown in the inset ($R^2 = .987$). UV–vis absorbance spectra for nanoclay compositions are shown in Figure 5b. As expected, no absorbance peak at 565 nm was observed for L_0. The calculated amount of TA released was 9.6 μg ml^{-1} for $LTA_{2.5}$, 19.5 μg ml^{-1} for LTA_4, and 26.1 μg ml^{-1} for LTA_5. Although the regression

only included three points, there was a strong presumption of linear relationship between the amount of TA initially present in the nanoclay composition and the amount released in solution after centrifugation (inlet).

Results from aPTT and thromboelastography measurements are summarized in Table 2. The aPTT for nanoclay compositions was significantly lower than that of the plasma control group (normalized at 100%), ranging between 33.3 ± 5.6 and 46.6 ± 14.7% and comparable to the Arista group (41.9 ± 17.9%). Thromboelastography recordings showed that the reaction time for composition $LTA_{2.5}$ (1.1 ± 0.1 min) was significantly lower than that of the plasma alone control group (1.8 ± 0.2 min) but not different from that of all other groups (1.3 ± 0.1 to 1.6 ± 0.2 min). The angle α, indicative of the celerity of clot formation was significantly lower for the plasma control group. It was significantly higher for composition LTA_4, compared to all other groups. The MA, reflective of clot strength, was significantly lower for the control group (50.9 ± 1.7 mm) and Arista positive control group (51.4 ± 1.9 mm), compared to all other groups. Composition $LTA_{2.5}$ had the highest MA (64.9 ± 0.7 mm) and it was significantly higher than that of LTA_5 (60.4 ± 0.6 mm), LTA_4 (63.9 ± 0.5 mm), or L_0 (61.8 ± 1.5 mm). The mean shear elastic modulus strength (G) was significantly lower for the plasma control (5.2 ± 0.3 Kd cm^{-2}) and Arista (5.3 ± 0.4 Kd cm^{-2}) groups, compared to nanoclay compositions. Group $LTA_{2.5}$ had the highest G value (9.2 ± 0.3 Kd cm^{-2}), which was significantly higher than that of all other groups with the exception of LTA_4 (8.8 ± 0.2 Kd cm^{-2}). The mean CI was also significantly lower for the control (3.2 ± 0.2) and Arista (3.4 ± 0.3) groups, compared to nanoclay compositions. Group $LTA_{2.5}$ had the highest CI value (5.5 ± 0.1), which was significantly higher than that of all other groups with the exception of LTA_4 (5.3 ± 0.1).

SEMs of the fibrin clots for the various compositions and controls are displayed in Figure 6. Both Arista and plain plasma controls (Figure 6a,b) exhibited thicker fibrin fibers than the nanoclay groups (Figure 6c–e). This difference is clearly seen at higher magnification (Figure 7) with composition LTA2.5 (Figure 7b) exhibiting thinner and denser fibers than Arista positive control (Figure 7a). Mean fiber diameters are summarized in Table 2. TA-doped compositions all exhibited significantly smaller fibrin fiber diameters ranging from 63 ± 15 to 70 ± 16 nm, compared to control plasma alone (112 ± 22 nm) or Arista control (134 ± 33 nm). Composition $LTA_{2.5}$ exhibited the lowest mean fibrin fiber diameter (63 ± 15 nm) and it was significantly lower than that of all other groups. There was no statistically significant difference in mean fiber diameter between compositions LTA_4 and LTA_5. The TA-free nanoclay composition exhibited a mean fiber diameter intermediate between TA-doped groups and control groups (85 ± 17 nm).

4 | DISCUSSION

4.1 | Impact of microstructure

THA control particles (Arista) did not show any open porosity, while all nanoclay microspheres exhibited a honeycomb microarchitecture with pores in the 3–6 μm range (Figure 2). A porous microstructure may be more favorable for blood factor concentration and provide a partial explanation for the generally faster clotting reaction times observed by thromboelastography for TA-loaded compositions compared to plain plasma control.

4.2 | TA loading and release

DTAs showed an endotherm at 449–461°C for the TA-loaded compositions that can attributed to the decomposition of TA since the TA-free composition did not. The endotherm at 300°C for Arista is attributed to the decomposition of polysaccharide. The exotherm at 780–784°C for all nanoclay compositions corresponds to the crystallization of magnesium silicate ($MgSiO_3$-PDF 19–768) as confirmed by XRD after DTA analysis (data not shown). The increase in interlayer d_{001} spacing for nanoclay compositions is in line with increasing TA loading as it has been shown that these nanocarriers incorporate payloads in the interlayer space. Meanwhile, solvating of the TA-loaded nanoclays with ethanol was accompanied by a release of TA and a significant decrease in interlayer spacing. Numerous studies have shown that the solvation of nanoclays with ethanol is accompanied by swelling upon contact of the clay minerals with the solvent,[24–26] solvation should therefore be associated with an increase in interlayer spacing. However, this behavior was only observed for the TA-free composition while all TA-loaded compositions exhibited a decrease in interlayer spacing. This result is in line with the observed release of TA from the interlayer space. The variations observed in interlayer spacing after TA release could be due to various degrees of remaining swelling.[26] This confirms that loaded LAP nanoclay compositions can readily release their payload even when solvated with ethanol.

Although in line with published values for LAP clays,[27] the SSA decreased by six to eight times after loading with TA. This can be explained by the fact that TA is known as a zwitterionic surfactant[28] and the addition of TA is likely to decrease the surface tension of LAP discs in solution and affect the final pore size and number within nanoclay microspheres. Meanwhile, UV–vis spectrometry analyses confirmed the release of between 9.6 and 26.1 μg ml^{-1} of TA by TA-loaded NMFs in solution with starting concentrations of NMFs of 10 mg ml^{-1}. Several studies have reported that a local TA concentration of 10 μg ml^{-1} of TA is sufficient to obtain 80% inhibition of plasminogen.[19,29,30] The prepared compositions fall therefore within the desirable pharmacological range for efficient antifibrinolytic effect. Furthermore, both aPTT and thromboelastography analyses demonstrated that the TA-loaded NMF compositions had a significant beneficial effect on the coagulation cascade. The aPTT is routinely used to evaluate coagulation abnormalities in the intrinsic pathway and to detect severe functional deficiencies in factors II, V, X, or fibrinogen. The hemostatic effect of TA has been demonstrated in numerous in vitro, preclinical and clinical studies.[18,31–33] Sarda et al.[32] reported on the development of hydroxyapatite with adsorbed TA and demonstrated local hemostatic activity with a lowered aPTT. More recently, Su et al.[33] reported on TA loading of starch microspheres and concluded on their potent hemostatic activity with a reduction in aPTT. Our results are in line with these studies and demonstrate that undoped nanoclay microspheres are associated with a reduction in aPTT by half, while TA-doped compositions led to a reduction in aPTT by about two thirds compared to the plasma control alone.

4.3 | Effect on coagulation cascade and fibrin network structure

Results from coagulation analyses and thromboelastography revealed that both doped and undoped nanoclay microsphere compositions not only reduced aPTT but also significantly increased the clot strength as expressed by parameters *MA* and *G* (shear elastic modulus

strength or clot strength).[22] However, only composition $LTA_{2.5}$ significantly reduced the reaction time *R*, compared to the controls and exhibited overall the most favorable combination of parameters. We postulate that this particular composition could correspond to the optimal concentration of TA for fastest coagulation and highest clot strength while higher concentrations did not lead to further improvements in coagulation behavior or tended to lower the clot strength and CI. It is interesting to note that the undoped nanoclay composition was associated with a significant decrease in mean fibrin fiber diameter, and denser clots compared to the control groups. Doping with TA led to further decrease in fiber diameter for all doped compositions compared to the undoped composition or controls groups.

TA is a synthetic analog of lysine and exerts its antifibrinolytic effect by binding to the lysine binding sites of plasminogen molecules, thereby preventing their conversion into active plasmin. As such, TA is recognized and administered as an antifibrinolytic agent.[29,34] Meanwhile, it is well established that the structure of the fibrin clot determines its fibrinolytic and viscoelastic properties.[35] Our results show that TA may also act on the fibrin structure and clot firmness. This is in agreement with previous studies on the effect of TA on the coagulation cascade and the structure of fibrin clots showing that thinner and denser fibrin fibers are more resistant to fibrinolysis and increase clot stiffness.[36,37] While the undoped nanoclay composition had a beneficial effect on clot formation and clot stiffness, TA-doped compositions led to thinner fibrin fibers and even stiffer clots which significantly increased the CI.

5 | CONCLUSIONS

NMFs either plain or doped with TA were successfully produced by freeze spraying and drying of LAP solutions. XRD studies revealed that TA was incorporated into the nanoclay structure and released in solution at levels expected for therapeutic action.

Both doped and undoped compositions led to a significant decrease in aPTT and increase in clot stiffness. These effects were more pronounced for the TA-doped microspheres and attributed to clot structure composed of thinner and denser fibrin fibers.

ACKNOWLEDGMENTS

This work was supported by Research Grant R21 DE028942 from the National Institutes of Health, National Institute of Dental and Craniofacial Research, Bethesda, MD 20892.

Funding information

National Institutes of Health, National Institute of Dental and Craniofacial Research, Grant/Award Number: R21 DE028942

DATA AVAILABILITY STATEMENT

The authors confirm that the data supporting the findings of this study are available within the article and its supplementary materials.

REFERENCES

1. Emilia M, Luca S, Francesca B, et al. Topical hemostatic agents in surgical practice. Transfus Apher Sci. 2011;45(3):305–311. [PubMed: 22040778]
2. Grotenhuis R, van Grunsven PM, Heutz W, Tan E. Prehospital use of hemostatic dressings in emergency medical services in the Netherlands: a prospective study of 66 cases. Injury. 2016;47(5):1007–1011. [PubMed: 26830121]
3. Wright JD, Ananth CV, Lewin SN, et al. Patterns of use of hemostatic agents in patients undergoing major surgery. J Surg Res. 2014;186(1): 458–466. [PubMed: 23993203]
4. Miloro M, Peterson LJ. Peterson's Principles of Oral and Maxillofacial Surgery. People's Medical Publishing House: Shelton, CT; 2012.
5. Baker SE, Sawvel AM, Zheng N, Stucky GD. Controlling bioprocesses with inorganic surfaces: layered clay hemostatic agents. Chem Mater. 2007;19(18):4390–4392.
6. Pourshahrestani S, Zeimaran E, Djordjevic I, Kadri NA, Towler MR. Inorganic hemostats: the state-of-the-art and recent advances. Mater Sci Eng C Mater Biol Appl. 2016;58:1255–1268. [PubMed: 26478429]
7. Gegel B, Burgert J, Gasko J, et al. The effects of QuikClot combat gauze and movement on hemorrhage control in a porcine model. Mil Med. 2012;177(12):1543–1547. [PubMed: 23397703]
8. Bennett BL, Littlejohn L. Review of new topical hemostatic dressings for combat casualty care. Mil Med. 2014;179(5):497–514. [PubMed: 24806495]
9. Roozbahani M, Kharaziha M, Emadi R. pH sensitive dexamethasone encapsulated laponite nanoplatelets: release mechanism and cytotoxicity. Int J Pharm. 2017;518(1–2):312–319. [PubMed: 28062364]
10. Ghadiri M, Chrzanowski W, Lee WH, Rohanizadeh R. Layered silicate clay functionalized with amino acids: wound healing application. RSC Adv. 2014;4(67):35332–35343.
11. Gaharwar AK, Mihaila SM, Swami A, et al. Bioactive silicate nanoplatelets for osteogenic differentiation of human mesenchymal stem cells. Adv Mater. 2013;25(24):3329–3336. [PubMed: 23670944]
12. Viseras C, Cerezo P, Sanchez R, Salcedo I, Aguzzi C. Current challenges in clay minerals for drug delivery. Appl Clay Sci. 2010;48(3): 291–295.
13. Wang SG, Wu YL, Guo R, et al. Laponite nanodisks as an efficient platform for doxorubicin delivery to cancer cells. Langmuir. 2013;29 (16):5030–5036. [PubMed: 23419072]
14. Gaharwar AK, Avery RK, Assmann A, et al. Shear-thinning nanocomposite hydrogels for the treatment of hemorrhage. ACS Nano. 2014;8(10):9833–9842. [PubMed: 25221894]
15. Thompson DW, Butterworth JT. The nature of laponite and its aqueous dispersions. J Colloid Interface Sci. 1992;151(1):236–243.
16. Gaharwar AK, Kishore V, Rivera C, et al. Physically crosslinked nanocomposites from silicate-crosslinked PEO: mechanical properties and osteogenic differentiation of human mesenchymal stem cells. Macromol Biosci. 2012;12(6):779–793. [PubMed: 22517665]
17. Valencia GA, Djabourov M, Carn F, Sobral PJA. Novel insights on swelling and dehydration of laponite. Colloids Interface Sci Commun. 2018;23:1–5.
18. Tengborn L, Blomback M, Berntorp E. Tranexamic acid—an old drug still going strong and making a revival. Thromb Res. 2015;135(2): 231–242. [PubMed: 25559460]
19. Astedt B Clinical pharmacology of tranexamic acid. Scand J Gastroenterol. 1987;22:22–25.
20. Schneider CA, Rasband WS, Eliceiri KW. NIH Image to ImageJ: 25 years of image analysis. Nat Methods. 2012;9(7):671–675. [PubMed: 22930834]
21. Ansari TM, Raza A, Rehman A. Spectrophotometric determination of tranexamic acid in pharmaceutical bulk and dosage forms. Anal Sci. 2005;21(9):1133–1135. [PubMed: 16363487]
22. Shaydakov M, Sigmon D, Blebea J. Thromboelastography StatPearls [Internet]. Treasure Island, FL: StatPearls Publishing; 2021 https://www.ncbi.nlm.nih.gov/books/NBK537061/
23. Conover W Practical Nonparametric Statistics. New York, NY: Wiley; 1999.
24. Dowdy RH, Mortland MM. Alcohol-water interactions on montmorillonite surfaces. I. Ethanol. Clays Clay Miner. 1967;15(1):259–271.

25. de Carvalho R, Skipper NT. Atomistic computer simulation of the clay-fluid interface in colloidal laponite. J Chem Phys. 2001;114(8): 3727–3733.
26. Murray RS, Quirk JP. The physical swelling of clays in solvents. Soil Sci Soc Am J. 1982;46(4):865–868.
27. Hegyesi N, Vad RT, Pukanszky B. Determination of the specific surface area of layered silicates by methylene blue adsorption: the role of structure, pH and layer charge. Appl Clay Sci. 2017;146:50–55.
28. Altaf M, Stoeckli-Evans H. A copper(II) paddle-wheel structure of tranexamic acid: dichloro-tetrakis mu-4-(ammoniomethyl) cyclohexane-1-carboxylato-O,O' dicopper(II) dichloride hexahydrate. Acta Crystallogr E. 2017;73:1421.
29. Nilsson IM. Clinical pharmacology of aminocaproic and tranexamic acids. J Clin Pathol Suppl (R Coll Pathol). 1980;14:41–47. [PubMed: 7000846]
30. Amin NH, Scudday TS, Cushner FD. Systemic versus topical tranexamic acid: how best to dose and administer. J Orthop Tech. 2017; 32(1):23–27.
31. Janbain M, Enjolras N, Bordet JC, et al. Hemostatic effect of tranexamic acid combined with factor VIII concentrate in prophylactic setting in severe hemophilia A: a preclinical study. J Thromb Haemost. 2020;18(3):584–592. [PubMed: 31782901]
32. Sarda S, Errassifi F, Marsan O, Geffre A, Trumel C, Drouet C. Adsorption of tranexamic acid on hydroxyapatite: toward the development of biomaterials with local hemostatic activity. Mater Sci Eng C: Mater Biol Appl. 2016;66:1–7. [PubMed: 27207032]
33. Su HT, Wei SD, Chen FP, Cui RH, Liu CS. Tranexamic acid-loaded starch hemostatic microspheres. RSC Adv. 2019;9(11):6245–6253.
34. Wu GJ, Mazzitelli BA, Quek AJ, et al. Tranexamic acid is an active site inhibitor of urokinase plasminogen activator. Blood Adv. 2019;3(5): 729–733. [PubMed: 30814058]
35. Weisel JW. Structure of fibrin: impact on clot stability. J Thromb Haemost. 2007;5:116–124. [PubMed: 17635717]
36. Chan LW, White NJ, Pun SH. A fibrin cross-linking polymer enhances clot formation similar to factor concentrates and tranexamic acid in an in vitro model of coagulopathy. ACS Biomater Sci Eng. 2016;2(3): 403–408. [PubMed: 29541687]
37. Carr ME, Alving BM. Effect of fibrin structure on plasmin-mediated dissolution of plasma clots. Blood Coagul Fibrinolysis. 1995;6(6): 567–573. [PubMed: 7578900]

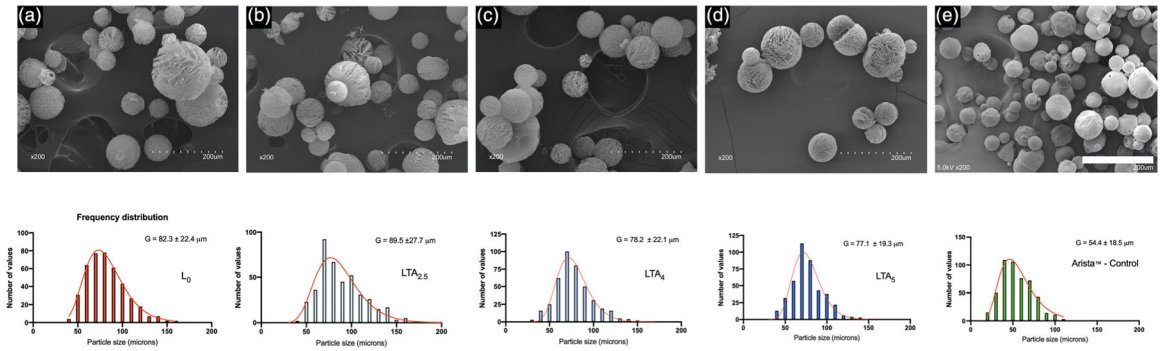

FIGURE 1.

Scanning electron micrographs and particle size frequency distributions of nanoclay and control microspheres. (a) L_0 undoped nanoclay composition, (b) $LTA_{2.5}$ nanoclay composition doped with 2.5 mg ml^{-1} tranexamic acid, (c) LTA_4 nanoclay composition doped with 4 mg ml^{-1} tranexamic acid, (d) LTA_5 nanoclay composition doped with 5 mg ml^{-1} tranexamic acid, and (e) Arista control. Bar: 200 µm

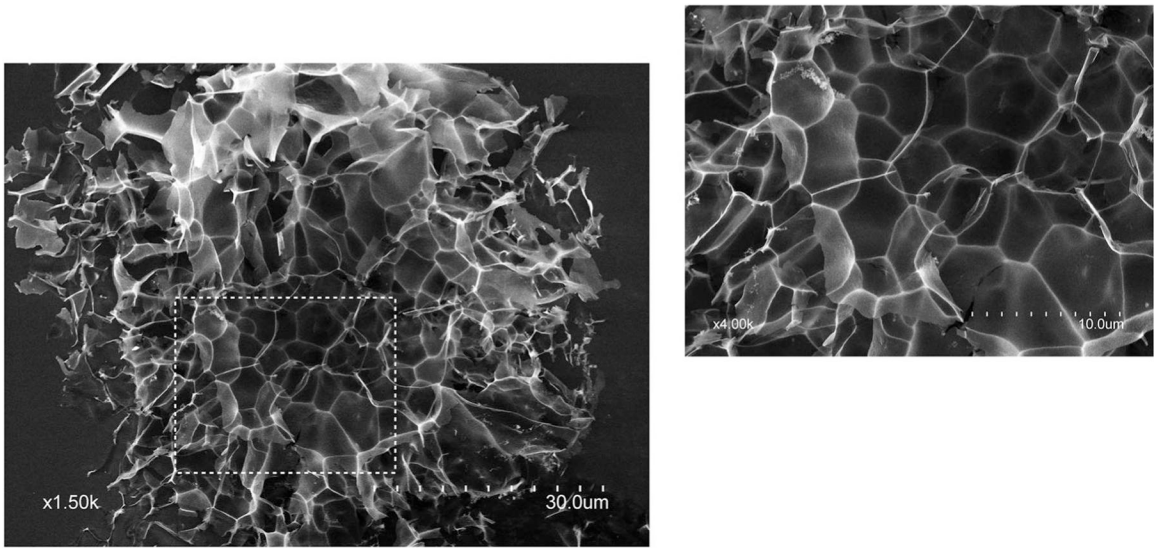

FIGURE 2.

Scanning electron micrograph showing the pore size and microstructure of nanoclay microsphere frameworks. Inset: higher magnification

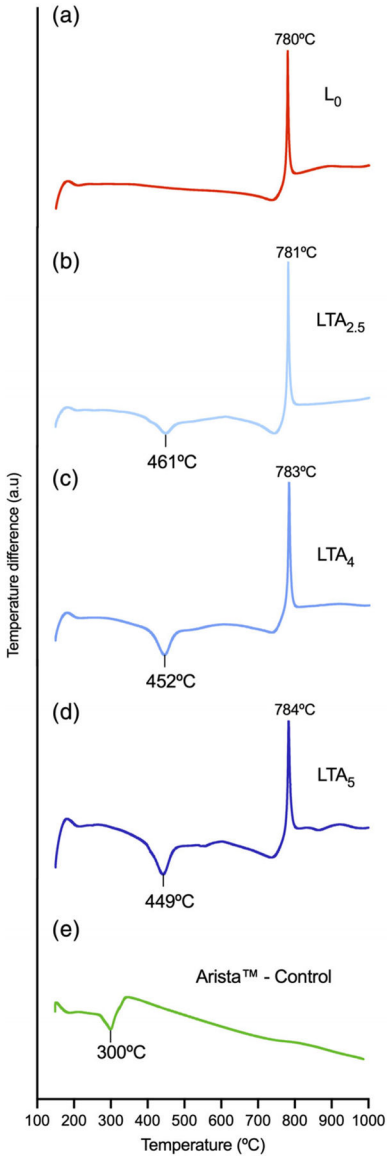

FIGURE 3.

Differential thermal analyses of the various compositions. (a) L_0, (b) $LTA_{2.5}$, (c) LTA_4, (d) LTA_5, and (e) Arista

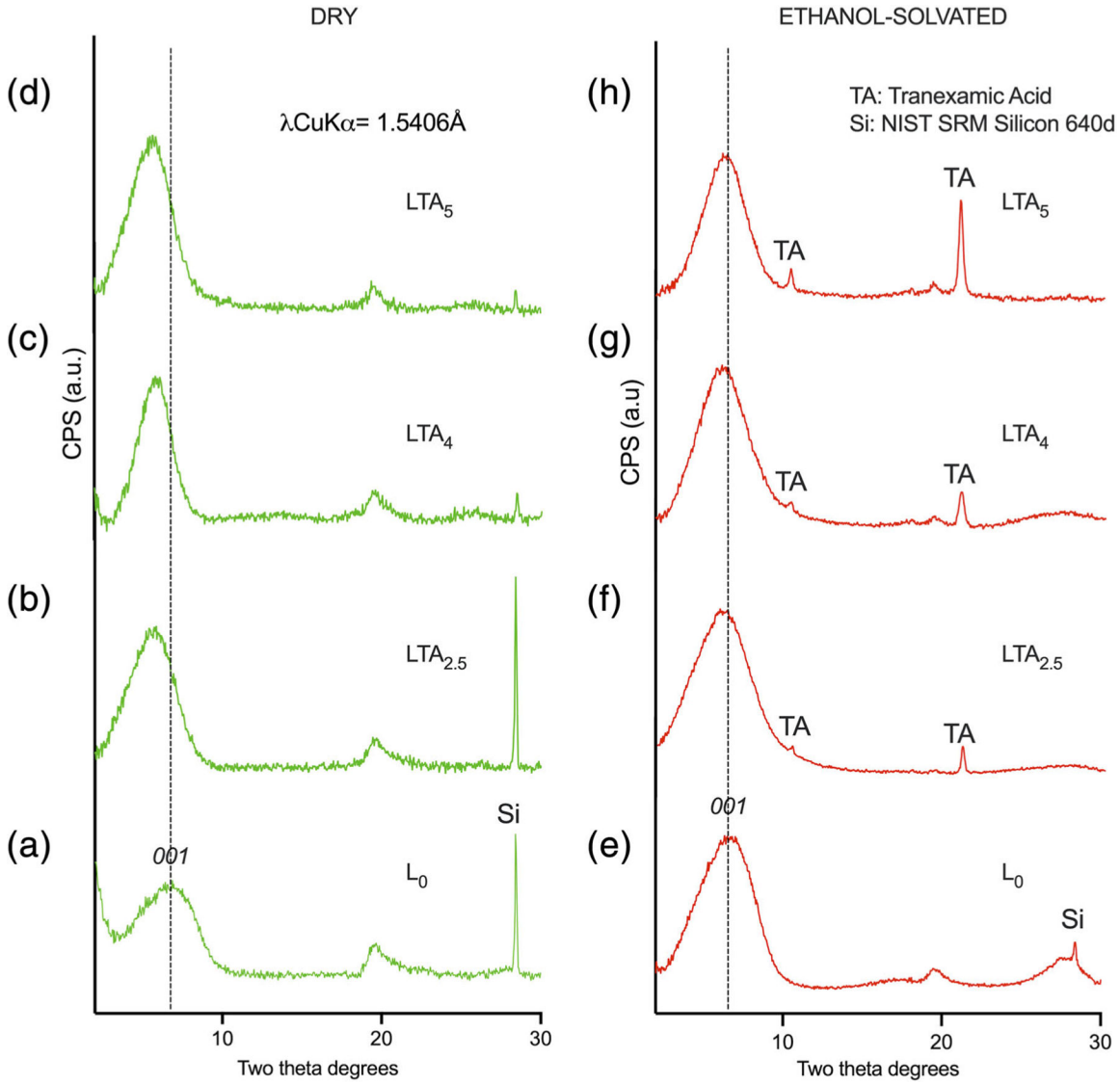

FIGURE 4.

X-ray diffraction patterns for the various compositions. Dry state: (a–d); solvated with ethanol: (e–g). (a–d) L_0 undoped composition; (b,f) $LTA_{2.5}$, (c,g) LTA_4; and (d,h) LTA_5

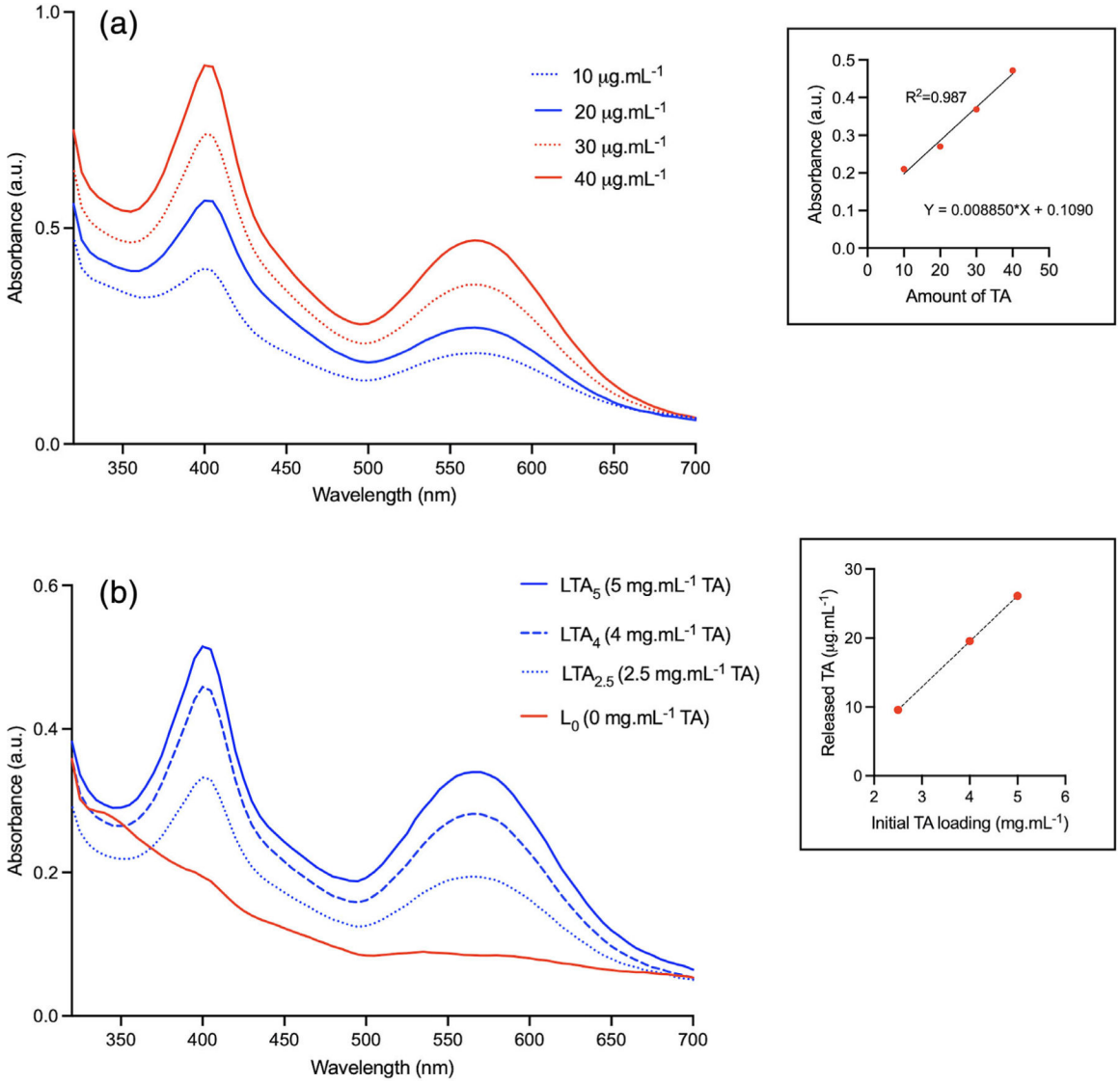

FIGURE 5.

Ultraviolet–visible (UV–vis) spectra. (a) Calibration curve for tranexamic acid; inset: linear regression. (b) UV–vis spectra for the various compositions; inset: regression for $LTA_{2.5}$, LTA_4, and LTA_5

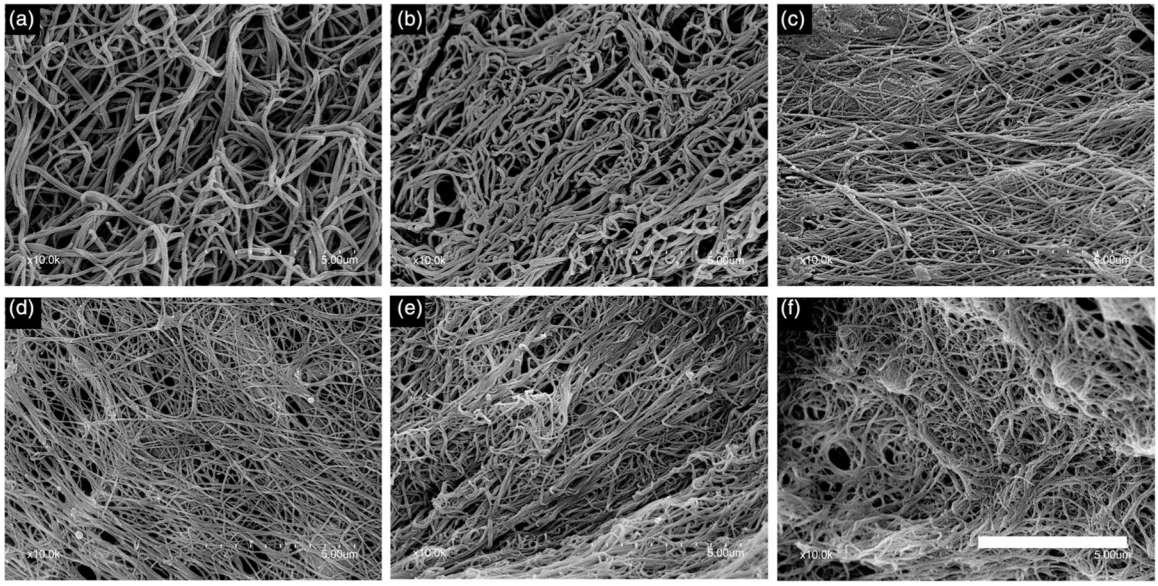

FIGURE 6.

Scanning electron micrographs of the fibrin clots for the various compositions. (a) Arista, (b) control plasma, (c) L_0, (d) $LTA_{2.5}$, (e) LTA_4, and (f) LTA_5. Bar: 5 μm

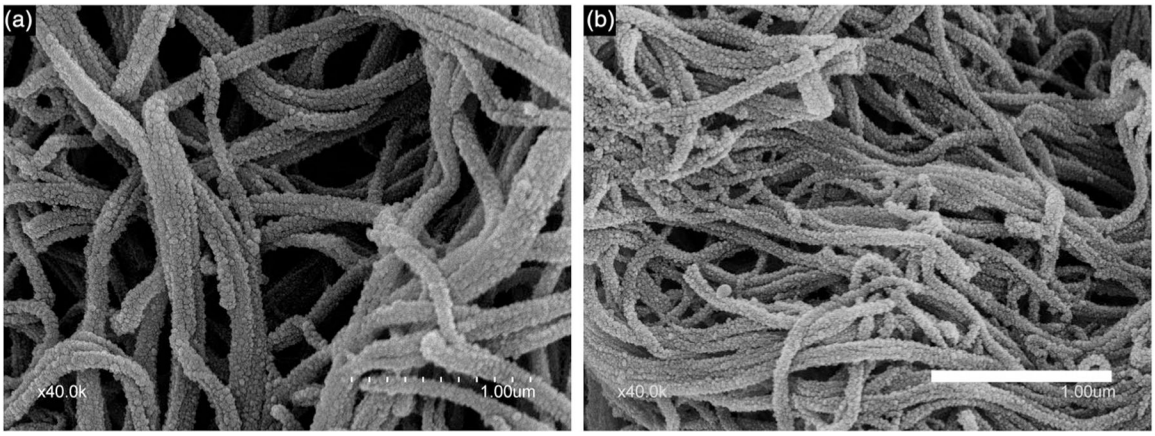

FIGURE 7.
Scanning electron micrographs of fibrin fibers. (a) Arista and (b) LTA_4. Bar: 1 μm

TABLE 1

Specific surface area and interlayer *d*-spacings of the various compositions with or without solvating with ethanol followed by drying at room temperature for 30 min

Composition	Specific surface area from BET adsorption profiles ($m^2\ g^{-1}$)	d_{001} (Å) (*SD*) (dried at 60°C for 15 min)	d_{001} (Å) (*SD*) (after solvating with ethanol and drying at room temperature for 30 min)
L_0	289	12.574 (0.033)[a]	13.760 (0.104)[b]
$LTA_{2.5}$	36	14.956 (0.075)[d]	14.580 (0.100)[c]
LTA_4	44	15.045 (0.092)[d]	14.347 (0.064)[c]
LTA_5	38	15.503 (0.096)[e]	13.980 (0.072)[b]

Note: Identical letters denote no statistically significant difference [$p > .05$] after adjustment for pairwise multiple comparisons of all eight groups.

Abbreviation: BET, Brunauer–Emmett–Teller.

TABLE 2

aPTT, thromboelastography parameters and mean fibrin fiber diameter for the various compositions, negative control and positive control (Arista)

Composition	aPTT (*SD*) (% control)	*R* (*SD*) (min)	Angle α (*SD*) (degrees)	Maximum amplitude (*SD*) (mm)	*G* (*SD*) (Kd cm^{-2})	CI (*SD*) (a.u.)	Mean fibrin fiber diameter (*SD*) (nm)
Control	100 (8.8)[a]	1.8 (0.2)[a]	82.3 (1.3)[a]	50.9 (1.7)[a]	5.2 (0.3)[a]	3.2 (0.2)[a]	112 (22)[a]
Arista	41.9 (17.9)[b]	1.6 (0.2)[ab]	83.1 (1.9)[b]	51.4 (1.9)[a]	5.3 (0.4)[a]	3.4 (0.3)[a]	134 (33)[a]
L_0	46.6 (14.7)[b]	1.4 (0.3)[b]	84.0 (1.7)[bc]	61.8 (1.5)[bc]	8.1 (0.5)[bc]	4.8 (0.1)[b]	85 (17)[b]
$LTA_{2.5}$	33.3 (5.6)[b]	1.1 (0.1)[b]	83.9 (1.5)[bc]	64.9 (0.7)[c]	9.2 (0.3)[d]	5.5 (0.1)[c]	63 (15)[c]
LTA_4	33.7 (7.1)[b]	1.3 (0.1)[b]	84.9 (0.5)[c]	63.9 (0.5)[bc]	8.8 (0.2)[cd]	5.3 (0.1)[bc]	64 (18)[d]
LTA_5	34.2 (8.4)[b]	1.4 (0.2)[b]	84.4 (0.6)[bc]	60.4 (0.6)[b]	7.6 (0.2)[b]	4.8 (0.2)[b]	70 (16)[d]

Note: Identical letters denote no statistically significant difference at the $p = .05$ level.

Abbreviations: aPTT, activated partial thromboplastin time; CI, coagulation index.

J Biomed Mater Res B Appl Biomater. Author manuscript; available in PMC 2023 February 01.